Chemical Engineering Journal 519 (2025) 165565

Contents lists available at ScienceDirect

Chemical Engineering Journal

journal homepage: www.elsevier.com/locate/cej

Advanced Fe-doped carbon xerogels as bifunctional electro-catalysts for targeted hydroxyl radical production and superior electro-Fenton pollutant removal in water

Lilian D. Ramírez-Valencia [a,*], Esther Bailón-García [a], Francisco Carrasco-Marín [a], Miguel A. Álvarez-Merino [b], Agustín F. Pérez-Cadenas [a]

[a] Materiales Polifuncionales Basados en Carbono (UGR-Carbon), Dpto. Química Inorgánica - Unidad de Excelencia Química Aplicada a Biomedicina y Medioambiente, Universidad de Granada, ES18071 Granada, Spain
[b] Department of Inorganic and Organic Chemistry, University of Jaén, 23071 Jaén, Spain

ARTICLE INFO

Keywords:
Bifunctional
Hydrothermal
iron carbide
Encapsulation
Electro-Fenton
Hydroxyl radicals

ABSTRACT

Bifunctional catalysts for H_2O_2 production via oxygen reduction reaction (ORR) and $OH^{\bullet}$ generation via Fenton reaction are fundamental for the development and optimization of Electro-Fenton technology. In this context, Fe-doped carbon xerogels have been synthesized by sol-gel polymerization under hydrothermal conditions, which allowed the efficient encapsulation of iron nanoparticles (Fe_3C-type crystalline species) within the carbon matrix. This strategy enabled control over the selectivity of the materials towards a three-electron pathway, favoring the direct production of hydroxyl radicals ($OH^{\bullet}$). Moreover, a good balance between graphitization degree and micro-mesoporous structure resulted in high electrochemical performance in ORR, reaching a kinetic current density as high as 11.56 mA/cm^2 at −0.45 V and 32.66 mA/cm^2 at −0.80 V. This remarkable performance was reflected in Electro-Fenton experiments, achieving 94% degradation of tetracycline after 8 h, demonstrating the bifunctional effectiveness of the synthesized catalysts.

1. Introduction

Conventional wastewater treatment systems are currently inadequate for the removal of a wide range of pharmaceutical compounds, which are continuously introduced into rivers, lakes, and aquifers. This persistent contamination represents a growing concern, posing risks to human health and threatening the integrity of aquatic ecosystems. Consequently, there is a pressing need to develop and implement more effective control measures and advanced treatment technologies. The Electro-Fenton process has emerged as a promising alternative to meet decontamination requirements, since it allows the in-situ generation of hydrogen peroxide (H_2O_2) at the cathode, which is subsequently transformed into $OH^{\bullet}$ by a Fenton-like catalyst (Fig. 1) [1]; $OH^{\bullet}$ radicals are highly oxidizing agents capable of degrading complex chemical compounds such as pharmaceutical waste [2,3]. This rapidly growing process offers several additional advantages that make it even more appealing. It can be operated at atmospheric pressure and ambient temperature, and it functions effectively over a much wider pH range, including near-neutral pH levels [4–6]. These features help reduce operating costs and minimize the handling risk associated with the storage and transport of H_2O_2.

To achieve a more efficient process, an active search is underway for catalysts with high electrochemical performance. Considering that Electro-Fenton process involves two main reaction (Fig. 1), two different types of catalyst are typically required: a) catalysts for the electrochemical reduction of oxygen, which can proceed through a two-electron pathway, reducing O_2 to H_2O_2; and b) Fenton-type catalysts (Such as Fe^{2+}, Cu^{+}, Co^{2+} or Mn^{2}) which convert H_2O_2 into $OH^{\bullet}$ [7]. For instance, Daneshvar et al. [8] and Labiadh et al. [9], employed the Electro-Fenton process to degrade an azo dye, using graphite felt as the electrocatalyst for the ORR to generate H_2O_2. To activate the H_2O_2 and produce $OH^{\bullet}$, both studies incorporated a secondary Fenton-type catalyst, Daneshvar et al. [8] added 10^{-4} M Fe^{3+} to the electrolyte solution, whereas Labiadh et al. [9] used pyrite (FeS_2) as the iron source. In both cases, a dye degradation efficiency of approximately 90% was achieved. On the other hand, Chen et al. [10] achieved methylene blue degradation using the Electro-Fenton process with two electrocatalysts, each serving a specific function. The first was nitrogen-doped graphene,

* Corresponding author.
E-mail address: liliandr@correo.ugr.es (L.D. Ramírez-Valencia).

https://doi.org/10.1016/j.cej.2025.165565
Received 10 April 2025; Received in revised form 30 June 2025; Accepted 1 July 2025
Available online 2 July 2025

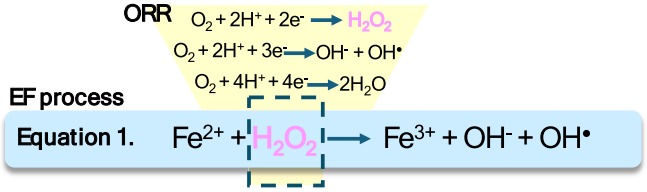

Fig. 1. Reactions process of ORR and Electro-Fenton.

employed for H_2O_2 production, which achieved a yield of 62%. The second electrocatalyst was an $FeSO_4$ solution at a concentration of 11.2 mmol L^{-1}, dissolved in a 0.10 mol L^{-1} electrolyte, resulting in a pollutant degradation efficiency of 97%. In comparison, Zhao et al. [11] reported a higher H_2O_2 yield of 81.9% using nitrogen-doped graphene foam as the catalyst. For the phenol degradation step via the Electro-Fenton process, they used FeOOH as the iron catalyst, demonstrating high system efficiency. More recently, Jiang et al. [12] investigated the degradation of sulfamethazine (SMZ) using a dual-electrocatalyst system. A key innovation in their approach was the incorporation of copper into graphite felt, used as the catalyst for the ORR. The presence of Cu improved electron transfer to O_2, thereby enhancing H_2O_2 generation. Additionally, their system facilitated the direct reduction of H_2O_2 to $OH^{\bullet}$, further boosting catalytic activity. The introduction of a second catalyst, FeS_2, significantly accelerated pollutant degradation, underscoring the synergistic effect between the catalysts. These variations in electrocatalyst design and operating conditions emphasize how both material selection and pollutant characteristics play critical roles in determining the overall efficiency of the Electro-Fenton process.

In light of the above, the study of separate catalysts for the Electro-Fenton process has been the predominant approach. On one hand, the ORR to H_2O_2 is carried out using carbon-based catalysts, as the ORR can follow different electron transfer pathways. It is desirable for the catalysts to favor specific routes: the 2-electron transfer for H_2O_2 generation or 3-electron transfer for hydroxyl radical production, while minimizing the 4-electron pathway, which leads to water formation and reduces process efficiency. Carbon-based electrocatalysts have demonstrated high selectivity towards $2e^-$ and $3e^-$ transfers [13–16], in addition to being abundant materials with excellent electrical conductivity and ease of functionalization through the incorporation of metals or heteroatoms, which significantly enhances ORR performance [17–19]. On the other hand, the H_2O_2 obtained from the ORR must be reduced to OH• radicals using another Fenton-type catalyst, generally an iron salt dissolved in the electrocatalytic solution. However, this strategy presents significant limitations, such as the need for continuous catalyst dosing, restriction to a narrow pH range, and difficulty in recovery and reuse over successive operational cycles [20,21].

A promising strategy to overcome these limitations involves immobilizing the active phases on solid substrates. Recently, the anchoring of Fenton-type catalysts onto carbonaceous materials has been investigated the same materials used as supports for the active phases in the oxygen reduction reaction enabling the development of bifunctional catalysts [22–24].

The design of carbon-based bifunctional catalysts that efficiently integrate both catalytic functions can offer several advantages: greater tolerance to pH variations, system simplification with more stable operation, reduction in H_2O_2 diffusion distance which increases reaction rate, decreased energy consumption, and overall improvement in contaminant degradation efficiency. In these types of bifunctional catalysts, it is essential to modulate the selectivity of the active phases for OH• generation. An effective strategy involves encapsulating metal nanoparticles such as Cu, Fe, or Co within the carbon matrix, which allows control over the exposure and stability of the active sites [25–30]. However, encapsulation processes can be costly, complex, and potentially polluting, posing an additional challenge for large-scale implementation.

In view of the context described, the main novelty of this work lies in the development of bifunctional catalysts in which iron carbide (Fe_3C), an active iron phase, is encapsulated in carbon xerogels (CX) via hydrothermal synthesis. This approach is economical, simple and versatile, unlike traditional methods, which are often tedious, costly and polluting. Furthermore, this methodology enables the production of xerogels with adjustable morphological, textural and chemical properties. This is crucial for modulating the selectivity of ORR towards the 2^- or 3^-electron pathway, which is essential for optimizing the production of $OH^{\bullet}$. Unlike previous studies that used separate catalysts or complex device architectures, this study proposes an integrated solution combining the ability to generate H_2O_2 and transform it into $OH^{\bullet}$ or even produce $OH^{\bullet}$ directly. This reduces costs and complexity while improving process efficiency. This strategy, which focuses on the use of carbon-based materials and the controlled encapsulation of active iron phases, represents a significant advance in the design of sustainable and efficient catalysts for advanced oxidation applications.

The performance of these materials as bifunctional catalysts was initially evaluated in ORR, in order to confirm their selectivity and catalytic activity. Subsequently, they were applied in the Electro-Fenton process using tetracycline (TTC), a broad-spectrum antibiotic, as the contaminant to be degraded. The selection of TTC as the target contaminant is justified by its high frequency of detection in wastewater and its remarkable environmental persistence, attributed to its chemical structure resistant to natural degradation and conventional water treatment processes [31]. This compound is one of the most widely used antibiotics worldwide due to its low cost and therapeutic efficacy, which has led to its extensive use in both human and veterinary medicine [32]. However, its persistent presence in water bodies represents a significant ecological and sanitary risk, as it can alter the aquatic microbiota, contribute to the proliferation of antimicrobial-resistant bacteria and accumulate in drinking and irrigation water sources, generating an emerging public health problem [33]. Compared to other emerging contaminants such as anti-inflammatory drugs, hormones or personal care products, TTC stands out not only because of its high toxicity and mobility, but also because of its resistance to biodegradation [34], making it a prime target for advanced environmental remediation technologies such as the Electro-Fenton process.

2. Experimental section

2.1. Synthesis of carbon xerogel with encapsulated iron nanoparticles

Iron-encapsulated carbon xerogels were synthesized by sol-gel polymerization of resorcinol (R) and formaldehyde (F) in the presence of iron (III) nitrate (Z) with a Fe theoretical percentage of 8 wt%, using ammonia (NH_4OH solution 25 wt%) (A) as a morphological catalyst in an ethanol (80 ml)-water (200 ml) mixture. The molar ratios used were R/F = 0.5 and R/A = 0.8.

In order to obtain different morphologies and Fe degree of encapsulation in carbon xerogels, the way in which the ammonia was introduced was varied according to Fig. 2, obtaining three different types of materials. CX-H-Fe-M1 in which the ammonia solution was added at the end over the R + F + H_2O + Ethanol+Z mixture, CX-H-Fe-M2 in which the ammonia was added drop by drop over the R + F + H_2O + Ethanol+Z adjusting up to a pH of 5 and CX-H-Fe-M3 in which a mixture of ammonia+ethanol+H_2O was added over the mixture R + F + H_2O + Z. All of this aiming to control the precipitation and nucleation of Fe hydroxide, and thus the properties of the carbon gels obtained. To obtain a control sample, an iron-free carbon xerogel was synthesized via hydrothermal synthesis. The synthesis of this reference sample, designated CX-H-B, employed the same molar ratios of R/F and R/A, as well as identical volumes of ethanol and water, as used in the iron-containing samples, and the mixture R + F + H_2O + Ethanol and ammonia solution was prepared as in the synthesis procedure of sample CX-H-Fe-M1.

Each mixture was placed in an autoclave and brought to a

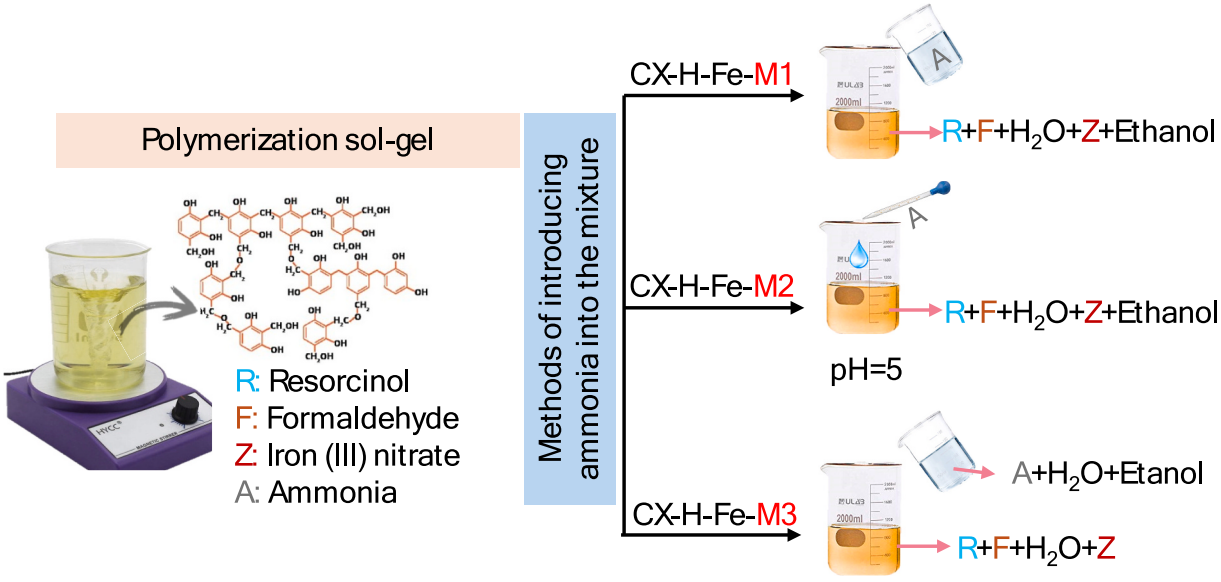

Fig. 2. Protocols for introducing ammonia in hydrothermal synthesis.

temperature of 100 °C for 24 h. Then, the obtained material was filtered and subjected to an exchange process with acetone for three days, changing the acetone several times. After completing the exchange of water for acetone, the material was dried in a microwave oven under an inert flow, using a power of 248 W at 1-minute intervals, until it reached a constant weight. Finally, the xerogel was carbonized at 850 °C for 2 h under a nitrogen flow (150 ml/min), using a heating ramp of 1.5 °C/min. An iron-free material was synthesized following the same hydrothermal method for comparison.

2.2. Textural and chemical characterization

Textural properties such as surface area (S_{BET}), micropore volume (W_0), average micropore width (L_0), mesopore volume (V_{meso}), total pore volume ($V_{0.95}$) and pore size distribution were determined from the data obtained by nitrogen adsorption at −196 °C. BET and Dubininin-Radushkevich (DR) equations were used for the determination of S_{BET} and W_0, L_0 respectively, the BJH method to obtain the pore size distribution and Gurvich rule ($V_{0.95}$-W_0) for determining V_{meso}.

The morphology of the samples was observed by scanning electron microscopy (HRSEM), using a AURIGA (FIB-FESEM) de Carl Zeiss SMT. The graphitization of the samples, together with the distribution of the iron particles were analyzed by transmission electron microscopy (TEM) on a LIBRA 120 Plus microscope. The average size of the iron particles was determined from TEM microphotographs using ImageJ 1.54f as software.

The crystalline structure was characterized by X-ray diffraction (XRD) using a Bruker D8 Venture diffractometer. X-ray diffraction patterns were recorded over a 2θ interval ranging from 5° to 75°. To calculate the average size of the metal crystals, the Debye-Scherrer equation was applied to the most intense diffraction peak, and for the interplanar distance the brag equation was used.

Raman spectroscopy was used to determine the degree of graphitization of the samples. A JASCO NRS-5100 scattering spectrophotometer with a 532 nm laser line was used. The quantitative surface chemical analysis of iron, carbon and oxygen was determined by X-ray photoelectron spectroscopy (XPS), using a Kratos Axis Ultra-DLD spectrometer equipped with an Al-Kα monochromator with a power of 600 W. The X-ray source is a 450 W Mg/Al double anode.

The thermal stability of the samples together with the actual doped iron content was determined by thermogravimetric analysis (TGA), using a SHIMADZU mod. TGA-50H equipment with vertical furnace design and a maximum accuracy of 0.001 mg.

2.3. Electrochemical characterization

Electrochemical impedance spectroscopy (EIS) was measured at room temperature in a two-electrode system, using 6 M KOH as electrolyte and using a Biologic VMP-300 potentiostat. The graphical analysis of the data obtained was represented by Nyquist plots.

ORR characterization was performed on a Biologic VMP multichannel potentiostat using a rotating disk-ring electrode (Metrohm AUTOLAB RDE-2, 3 mm glassy carbon tip). 20 µl of dye of the sample to be analyzed was deposited on the disk as working electrode; the dye consists of 5 mg of sample dispersed in 1 ml of a Nafion solution (1 ml Nafion in 9 ml water); a Pt foil together with an Ag/AgCl electrode served as counter and reference electrodes respectively.

Cyclic voltammetry (CV) experiments were carried out on two types of solutions: a 0.1 M KOH solution saturated with oxygen and a 0.1 M KOH solution O_2 degassed by bubbling with N_2. The potential was swept at a rate of 50 mV/s, ranging from 0.4 V to −0.8 V vs Ag/AgCl, while the ring rotating disk electrode (RRDE) was rotated at 1000 rpm. Linear scanning voltammetry (LSV) experiments were carried out in a 0.1 M solution of KOH saturated with oxygen, varying the rotational speed from 500 rpm to 3500 rpm. These experiments were performed over a potential range of 0.4 V to −0.8 V vs. Ag/AgCl, with a sweep speed of 5 mV/s.

The treatment of the LSV data (disk data) fitted to the Koutecky-Levich model allowed the determination of the number of electrons transferred (n) and the kinetic current density (J_k) using Eqs. (1) and (2). The onset overpotential was determined from the point where the linear regime begins in the Tafel diagram. The exchange current density was obtained by extrapolation from the Tafel diagram [35]. On the other hand, the percentage of H_2O_2 produced was calculated from the data obtained from the platinum ring currents according to Eq. (3).

$$\frac{1}{j} = \frac{1}{jk} + \frac{1}{B\omega^{0.5}} \tag{1}$$

$$n = \frac{5 \bullet B \bullet \nu^{1/6}}{F \bullet (D_{o2})^{2/3} \bullet C_{O2}} \tag{2}$$

$$H_2O_2\% = 100 \bullet \frac{2 \bullet \frac{I_R}{N}}{I_D - \frac{I_R}{N}} \tag{3}$$

where F is the Faraday constant, D_{O2} and C_{O2} are the oxygen diffusion coefficient (1.9×10^{-5} cm^2 s^{-1}) and oxygen concentration (1.2×10^{-6} mol cm^{-3}), respectively; ν is the viscosity (0.01 cm^2 s^{-1}); j is the current density; jk is the kinetic current density; ω correspond to the rotation speed [36]. I_R and I_D are the ring and the disk currents, respectively and N is the collection efficiency of the RRDE ($N = 0.245$) [37].

2.4. Electro-Fenton process

In order to eliminate the adsorption contribution in the Electro-Fenton process, the adsorption isotherm for each sample was determined to know the equilibrium concentration. In the Electro-Fenton system, 40 mg of catalyst is used in contact with 100 ml of electrolyte (0.5 M Na_2SO_4 with tetracycline). Therefore, 4 mg of catalyst in 10 ml of the same electrolyte with tetracycline concentrations of 50, 40, 30, 20 and 10 mg/L were used for adsorption tests. The solutions were kept in a thermal bath with a continuous stirrer at 25 °C for 24 h, sufficient time to reach equilibrium. The resulting isotherms were fitted with the Freundlich model using STATISTICA 7.0 software (Fig. 3S).

The Electro-Fenton system consisted of a cell composed of three electrodes: Ag/AgCl as reference electrode, a platinum plate as counter electrode and the carbon material (CX-H-Fe-x, x is the preparation method) as working electrode, which was made up of a homogeneous paste made of the carbon xerogel and a binder (polytetrafluoroethylene PTFE) in a ratio of 9:1. For the preparation of the working electrode, 40 mg of this paste was deposited on a graphite sheet in an area of 2. 5 × 1 cm^2. The cell was controlled by means of a Biologic VMP multichannel potentiostat (BioLogic Science Instruments).

For the Electro-Fenton experiments, first the working electrode was saturated in the dark for 24 h in a solution composed of 0.5 M Na_2SO_4/tetracycline (target contaminant) until a concentration of 14 mg/L was obtained, according to adsorption isotherms made for each material. The solution was then saturated for 30 min with a constant bubbling of O_2 and once the saturation was finished, the reaction was started by applying a voltage of −0.45 V in a potentiostatic mode without stopping bubbling O_2. During the tests, 1 ml aliquots were periodically withdrawn at specific time intervals, and the tetracycline concentration was immediately measured using a UV spectrophotometer model UV-2600i Shima, registering the TTC maximum absorption at the wavelength of 357 nm.

After completion of the Electro-Fenton reaction, the electrolyte solution was collected to analyze the iron leaching. This analysis was performed by Inductively Coupled Plasma Emission Spectroscopy (ICP-OES) with the ICP-OES spectrometer PERKIN-ELMER OPTIMA 8300, located in the Analysis and Structure Determination Service of the Scientific Instrumentation Center (CIC) of the University of Granada.

Additionally, toxicity tests were performed using the standardized biotest for luminescence inhibition of *Vibrio fischeri* bacteria (UNE/EN/ISO 11345-2), both before and after Electro-Fenton process. The tests were conducted with the LUMIStox 300 System and a LUMIStherm incubator. Toxicity was assessed based on the percentage of luminescence inhibition after 15 and 30 min of exposure (I %), using a saline stock solution as the control.

The TTC Electro-Fenton kinetics were studied using the following first and second order kinetic model Eqs. (4) and (5):

$$[C]_f = [C]_0 e^{-k_1 t} \tag{4}$$

$$\frac{1}{[C]_f} = k_2 t + \frac{1}{[C]_0} \tag{5}$$

$[C]_f$ and $[C]_0$ represent the concentration of TTC (mg L^{-1}) at t (min). k_1 (min − 1) and k_2 (L mg − 1 min − 1) are the first and second-order reaction rate constants, respectively, which were obtained by least squares.

3. Results and discussion

To evaluate the potential of the synthesized bifunctional catalysts for Electro-Fenton applications, their physicochemical and electrochemical properties were thoroughly analyzed, with particular attention to the effect of Fe_3C encapsulation and the structural features influencing ORR activity, hydroxyl radical generation and Electro-Fenton process.

3.1. Physicochemical characterization of iron-doped-carbon xerogels

The morphology of the carbon xerogels was analyzed by SEM (Fig. 3). In the iron-free sample, adjacent and symmetrical spheres of 1.0 μm of size were obtained (Fig. 3a), which is attributed to the hydrothermal synthesis process. During this process, individual emulsion droplets are formed, composed of a bond between hydrogen from water, ethanol, resorcinol, and formaldehyde [38–41]. Within these droplets, RF polymerization occurs, facilitated by the presence of ammonia as a basic catalyst, which also acts as a structural agent guiding the formation of the spheres [42,43]. However, when iron is introduced into the synthesis, the morphology of the spheres changes (Fig. 3b). This behavior can be explained to the catalytic role of iron in the RF polymerization, which accelerates the formation of polymer spheres. This rapid polymerization may interfere with the formation of the bond between ethanol, hydrogen, and RF, resulting in the melting of individual droplets during the synthesis process and thus eventually forming non-symmetrical fused semi-spheres as observed for sample CX-H-Fe-M1. Additionally, the manner of ammonia introduction during synthesis was found to influence the final morphology of the samples. By employing methodology two, where ammonia was added dropwise to

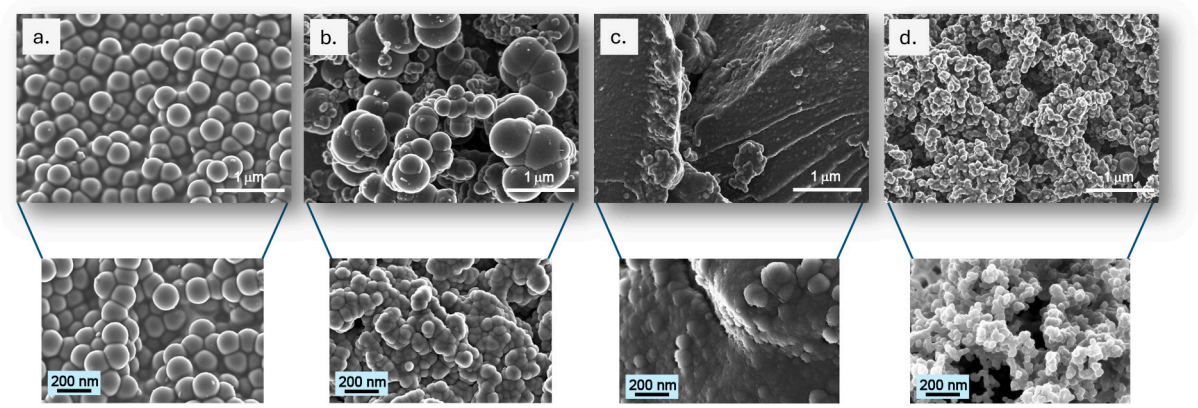

Fig. 3. SEM images of carbon xerogels synthetized with different morphologies a) CX-H-B, b) CX-H-Fe-M1, c) CX-H-Fe-M2 and d) CX-H-Fe-M3.

the mixture of ethanol, water and RF until a pH of 5 was obtained, sample CX-H-Fe-M2 exhibited a compact and amorphous morphology (Fig. 3c). Methodology three, which involved the addition of ammonia dissolved in water and ethanol to a mixture of RF and water, resulted in the formation of a coral-like morphology, composed of smaller particles (Fig. 3d). These observations confirm that ammonia plays a pivotal role in influencing the morphology of xerogels.

TEM confirmed how the structure of the xerogels was modified compared to the iron-free sample (Fig. 4). It was also observed that the preparation method influenced not only the structural change, but also the distribution of doped iron, the metal particle size and the degree of graphitization.

In samples CX-H-Fe-M1, CX-H-Fe-M2, CX-H-Fe-M3 graphitic clusters are observed distributed throughout the carbonaceous matrix due to the introduction of iron nanoparticles that catalyze the formation of these clusters [44]. The difference resides in the doped iron particle size in each of the materials and therefore in their distribution. Iron particles of small size, around 12 nm, highly dispersed within the carbon matrix are observed for CX-H-Fe-M2 (Fig. 4b), which allows the formation of more graphitic cluster. On the other hand, CX-H-Fe-M1 and CX-H-Fe-M3 samples have a larger particle of size of 18.2 and 16.4 nm respectively. Note that for CX-H-Fe-M2 and even CX-H-Fe-M1, although to a lesser extent, almost all the carbon matrix is composed by graphitic clusters whereas for CX-H-Fe-M3 part of the carbon matrix is absent of these graphitic clusters. These clusters must affect the conductivity of the samples and, therefore, their behavior as electrodes.

The degree of graphitization was also corroborated by XRD and Raman. Firstly, the XRD diffractograms of the samples are presented in Fig. 5a. Two intense peaks were identified for CX-H-B at $2\theta = 23.46°$ and 43.9° corresponding to the crystallographic planes of graphite (002) and (100), respectively. These peaks become narrower and are displaced to larger angles (2θ = 25.74°, 25.9° and 25. 82° for M1, M2 and M3 samples, respectively) in iron doped samples which manifest the increase of graphitization degree of these samples due to the development of graphitic clusters which are consistent with TEM observations. The displacement is also confirmed by calculating the interlaminar spacing d_{002} using the Bragg Eq. (1), explained in the experimental section. The results are summarized in Table S1. It is observed that the value of d_{002} for the iron-doped samples is lower compared to the CX-H-B. It is also important to highlight that the highest displacement and best defined and narrowest peak is observed for CX-H-Fe-M2, which is also the sample in which the best iron dispersion and thus, graphitic clusters were observed by TEM confirming the highest graphitization degree of this sample. In addition to the graphite peaks, a pattern of the orthorhombic crystalline structure of Fe_3C is also observed for CX-H-Fe-M1, CX-H-Fe-M2 and CX-H-Fe-M3 samples, which consists of nine main peaks at 37.6°, 37.7°, 42.9°, 43.7°, 44.6°, 45.0°, 45.9°, 48.6°, and 49.1° corresponding to (121), (210), (211), (102), (220), (031), (112), (131), and (221) planes, respectively [45,46]. The iron particle size in the different samples was calculated (Table S1), confirming that the M2 synthesis methodology allows obtaining small Fe particles, compared to the M1 and M3 methodologies in which a larger Fe crystal size was obtained.

On the other hand, the Raman spectra are shown in Fig. 5b, where the D band (I_D), which represents the degree of defects, and the G band (I_G), which indicates the degree of graphitization, have been identified. To properly characterize the degree of graphitization, three parameters extracted from the Raman data were considered. First, the I_D/I_G ratio is used to determine the order of the materials, with a low value being indicative of a high degree of graphitization [47]. Second, the bandwidth D (W_D) was calculated since the I_D/I_G ratio also depends on the size of the graphite crystallite and thus only is indicative of the degree of graphitization for samples with similar graphite crystallite sizes; a wide W_D may indicate a low degree of graphitization [48]. Finally, the appearance of a third peak in the Raman spectrum, corresponding to the 2D band, is also an indication of a high degree of graphitization [49]. In the case of the CX-H-B sample, the 2D band peak is absent. However, this peak becomes evident for the iron doped samples, indicating in the first instance a high degree of graphitization. On the other hand, although the I_D/I_G ratio for all the samples does not vary significantly, the W_D parameter allows to clarify that indeed the introduction of iron improves the degree of graphitization since this value is decreased, with respect to the CX-H-B sample (Table S1). In particular, the sample synthesized by methodology two (CX-H-Fe-M2) is observed as one of the most graphitic samples since presents the lowest values of I_D/I_G and W_D as it was also pointed out by TEM.

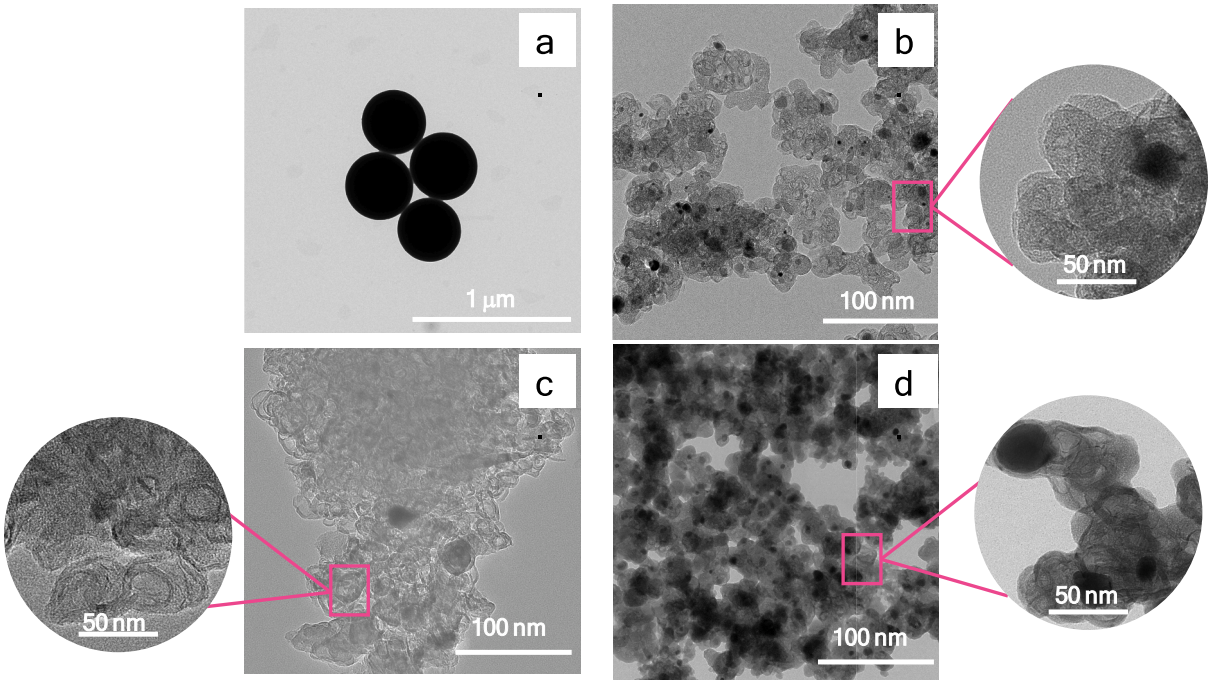

Fig. 4. TEM images of carbon xerogels synthetized with different morphologies a) CX-H-B, b) CX-H-Fe-M1, c) CX-H-Fe-M2, d) CX-H-Fe-M3.

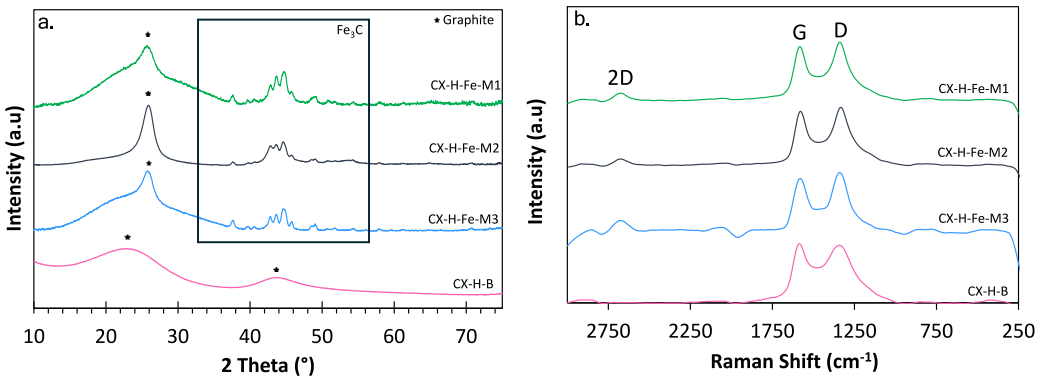

Fig. 5. a) XRD patterns of CX-H-Fe-X and CX-H-B samples. b) Raman spectra of pure (CX-H-Fe-X and CX-H-B samples.

Accordingly, just as the method of synthesis and the introduction of iron influenced the final morphology, the iron distribution and the degree of graphitization of the materials which is important as for electrodes materials for Electro-Fenton. However, accessibility to the active site is also quite important. Thus, the textural properties of the different samples were analyzed using nitrogen adsorption isotherms at −196 °C. The N_2 adsorption and desorption isotherms are plotted in Fig. 6 and the data are summarized in Table S1.

The shape of the isotherm of the CX-H-B sample corresponds to a type I isotherm according to the IUPAC classification, characteristic of microporous materials, which is attributed to the isolated nanospheres inside which numerous micropores are developed. On the other hand, the iron doped samples have a hybrid type I-IV isotherm, with a marked hysteresis cycle from a P/P_0 of 0.4 to 1, characteristic of mesoporous materials, and a high adsorption of N_2 at low relative pressures, indicating the presence of micropores [50]. The pore size distributions of the different samples were calculated employed BJH method and are shown in Fig. 6 b-d. It is observed that for samples CX-H-Fe-M1, CX-H-Fe-M2, CX-H-Fe-M3, the mean mesopore size is 3.5, 3.9 and 3.7 nm respectively. It is important to highlight that CX-H-Fe-M2 presents the lowest surface area a mesopores volume due to the compact and amorphous morphology observed by SEM images (Fig. 3c). Higher mesopores volume is obtained for CX-H-Fe-M1 and CX-H-Fe-M3 samples, especially for the last one, ascribed to their morphology composed by fused primary particles (smaller for M3 sample). In carbon gels, microporosity is typically attributed to the intraparticle voids, while mesoporosity and macroporosity are associated with the interparticle voids. In the case of undoped sample, isolated nanospheres are obtained which manifests high volume of micropores and absence of mesoporosity. In CX-H-Fe-M1 and CX-H-Fe-M3 samples, the fusion of primary spherical particles leaves mesoporosity. Since a more homogeneous distribution of smaller primary particles are obtained for CX-H-Fe-M3 than for CX-H-Fe-M1, higher mesopore volume is obtained.

Regarding the chemical composition of the materials, first a TGA was performed to determine the real percentage of doped iron in the samples (Table S2). The materials synthesized by methodologies M1 and M3 obtained a value close to the theoretical doped percentage, on the other hand, the sample synthesized by methodology two (CX-H-Fe-M2) has an iron percentage lower than the theoretical one, this discrepancy implies that the methodology used for this case does not allow the effective incorporation of the iron particles in the carbon matrix. It is important to remark that in spite of the much lower amount of iron incorporated in

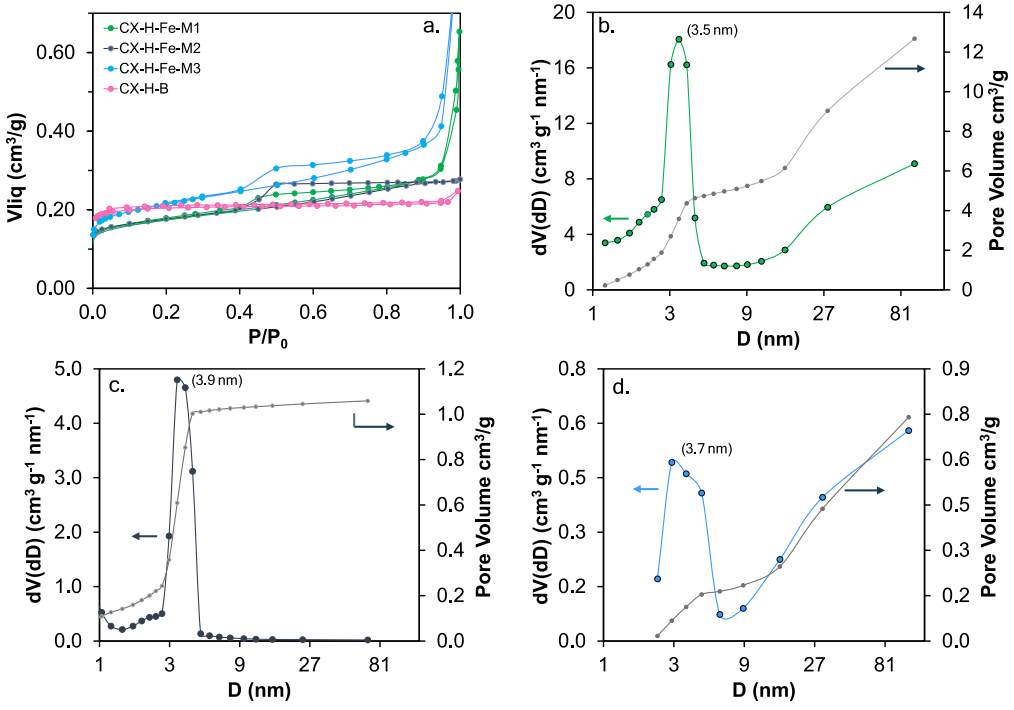

Fig. 6. a) N_2 adsorption isotherms, Pore size distribution and total cumulated volume (BJH method) of a) CX-H-Fe-M1, b) CX-H-Fe-M2 and c) CX-H-Fe-M3.

the material, this is the most graphitic sample that could be explained in terms of iron dispersion. This samples presents the highest Fe dispersion, that is, the lowest particle size and consequently, the amount of active phase for graphitic cluster growth could be high enough for the graphitization process. Finally, the introduction of a high percentage of iron during the synthesis in samples CX-H-Fe-M1 and CX-H-Fe-M3, affects the thermal stability respect to sample CX-H-B due to iron can catalyze the thermal decomposition reaction leading to a lower degradation temperature (Fig. 7).

The distribution of iron and other elements on the surface of the materials was analyzed by XPS (Fig. 8). Regarding the C_{1s} spectrum region (Fig. 8a), six peaks are required which were assigned to C═C (248.5 eV), C—C (284.3 eV), C—O (286.6 eV), C═O (288.3 eV), COO- (289.5 eV) type bonds and a π-π* satellite peak (291.2 eV). In the case of the O_{1s} spectrum (Fig. 8b), it was split into two peaks corresponding to C═O (532.3 eV) and C—O (533.5 eV). The C_{1s} and O_{1s} regions of the iron doped samples have a similar surface chemistry to the sample without iron, also the carbon and oxygen content do not change significantly with respect to the CX-H-B sample (Table S2), indicating that the introduction of iron does not alter the surface chemistry. As for the iron spectrum, no strong Fe signal is detected, indicating that most of the metallic particles are embedded in the carbon matrix.

3.2. Electrochemical characterization

EIS was performed and Nyquist diagrams are presented in Fig. 9a. In these diagrams, it is possible to identify the system resistance (R_S) [51], the electron transfer resistance (R_{CT}), which is observed as a semicircle in the zoomed-in Fig. 9a, and the internal resistance (R_Σ), which measures the impedance against the movement of ions within the electrode structure [52]. EIS measurements were performed on a two-electrode system using 6 M KOH solution as electrolyte. A low R_S is observed for the three samples, similar among them, indicating a good electrical contact between the electrolyte, the working electrode and the current collectors, making the systems used for each sample comparable. On the other hand, it was found that the resistance R_{CT} of sample CX-H-Fe-M2 is lower compared to the other two samples, which can be attributed to the high degree of graphitization of this sample, which facilitates electron conduction. However, its resistance R_Σ is higher, as reflected in the decrease of the slope of the straight line in the high frequency region of the Nyquist diagram. This indicates diffusion problems, mainly due to the low mesoporosity, which prevents effective ion transport inside the electrode. In contrast, sample CX-H-Fe-M3, which has a larger volume of mesopores, exhibits the lowest R_Σ resistance, followed by sample CX-H-Fe-M1.

Cyclic voltammetry (CV) was also performed under a flow of nitrogen or oxygen, using a three-electrode system in which a rotating RDEE disk was used as the working electrode. The CVs in N_2 of the materials are shown in Fig. 9b. The area under the curve of the CVs represents the energy storage capacity, known as capacitance. It was observed that sample CX-H-Fe-M2 presented the lowest area compared to the other samples, despite being the most graphitic. However, capacitance does not only depend on the electrical conductivity of the materials, but also on the surface characteristics, such as the type of porosity. Micropores are responsible for enabling the formation of the electrical double layer, while mesopores facilitate efficient diffusion of the electrolyte ions through the carbon matrix to the micropores [53,54]. Therefore, in the case of the CX-H-Fe-M2 sample, its lower capacitance is due to a reduced volume of mesopores compared to the CX-H-Fe-M1 and CX-H-Fe-M3 samples, which limits the effective diffusion of the electrolyte ions into micropores. The above is in line with what has been seen in EIS.

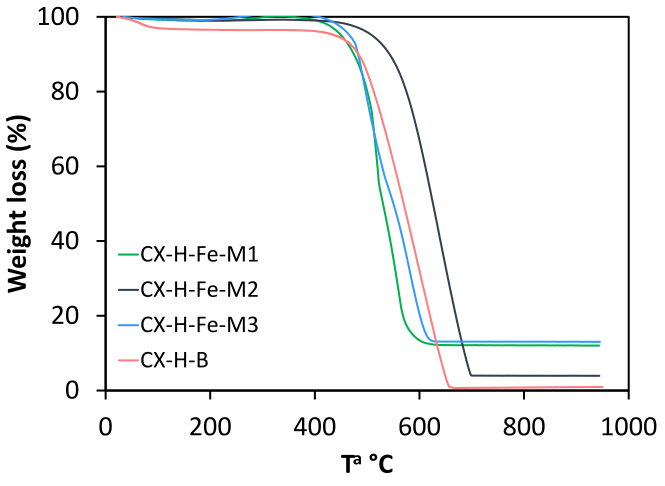

Fig. 7. TGA profiles of Fe-doped carbon samples.

Regarding the CV in oxygen (Fig. 10), it can be observed that in the voltammograms of the samples with the highest iron content, around 8% (CX-H-Fe-M1 and CX-H-Fe-M3), there is a peak at a potential of −0.45 V vs. Ag/AgCl, which corresponds to the redox process of iron going from Fe^{2+} to Fe^0 [55]. On the other hand, comparing the CVs in oxygen with respect to those made in nitrogen, an increase in the current density at a potential of −0.20 V vs. Ag/AgCl is identified, which indicates that the three samples analyzed have an activity towards the electro-reduction of oxygen. However, this increase in the current density is higher for samples CX-H-Fe-M1 and CX-H-Fe-M3 compared to sample CX-H-Fe-M2. This difference in activity may be due to factors such as the percentage of doped iron and the accessibility of the reagents to the active sites, bearing in mind that in all three samples the iron is embedded in a carbon matrix, so that open or closed porosity may affect the electrochemical performance of the ORR.

To further explore the influence of the physicochemical properties of the materials on their electrochemical performance, the kinetic current density (J_k), the reaction onset potential ($E_{(onset)}$), and the reaction mechanism were evaluated by determining the number of electrons transferred (n). These parameters were determined by linear sweep voltammetry (LSV) with a rotation speed range from 500 to 3500 rpm (Fig. 1S) and the comparison of LSV between samples were plotted at 3500 rpm and are shown in Fig. 11a. The data were fitted to the Koutecký-Levich equation and finally the results are collected in the Table 1.

For CX-H-Fe-M1 and CX-H-Fe-M3 samples, an increase in current density and a decrease in reaction onset potential was observed compared to sample CX-H-B. This can be largely attributed to the high iron content introduced into the carbon matrix during the synthesis. In addition, when considering the results observed in Raman analysis, it was found that these two samples were not as graphitic as the CX-H-Fe-M2 sample. However, although a highly graphitic sample may have a high electrical conductivity, it has the disadvantage of not having enough active sites, such as those formed in materials with more defects [56]. Therefore, the samples synthesized by methodologies 1 and 3 achieved a good balance, obtaining an optimal degree of graphitization and an abundant amount of active sites, resulting in superior electrochemical performance. On the contrasted side, CX-H-Fe-M2 sample, containing approximately 6% less iron, showed an improvement in current density compared to the control sample. However, its activity was significantly lower than that of samples CX-H-Fe-M1 and CX-H-Fe-M3, and it did not show a decrease in onset potential. This demonstrates that the synergy of a material to achieve high electrochemical activity does not depend solely on a high degree of graphitization.

Another relevant factor for the electrochemical activity was the morphological structure and porosity of the samples. The morphology of the CX-H-Fe-M2 sample consists of compact carbon xerogel blocks with low mesoporosity, which limits the access of the reagents to the active sites. In contrast, CX-H-Fe-M1 and CX-H-Fe-M3 samples, with a more open morphology and greater mesoporosity development, facilitated better reagent access. This behavior observed in LSVs coincides with the

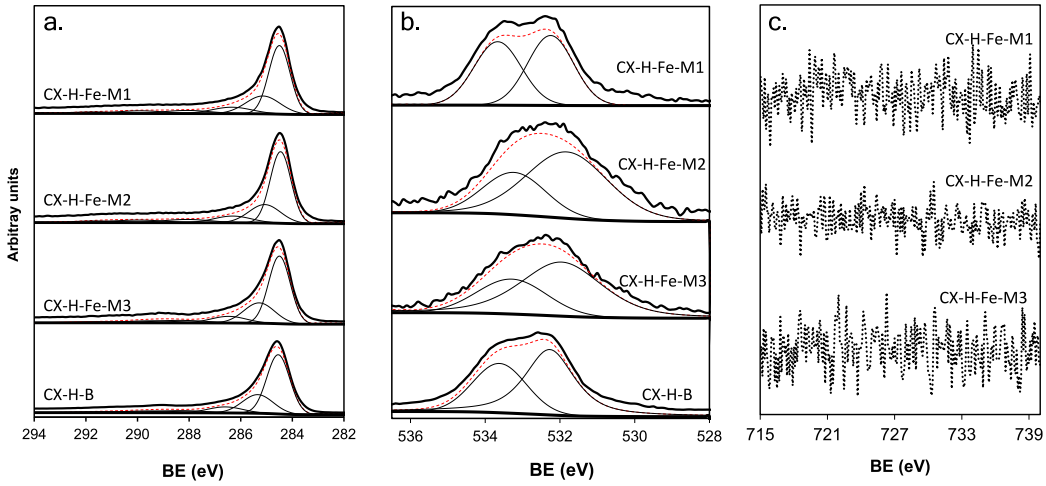

Fig. 8. XPS patterns of the a) C1s, b) O1s and Fe2p regions.

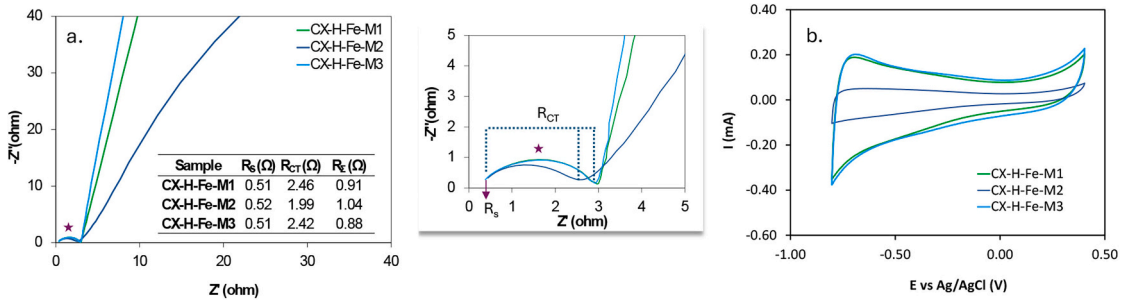

Fig. 9. a) Nyquist plot of CX-H-Fe-X samples b) Cyclic voltammogram in N_2-saturated KOH solution at 1000 rpm and 50 mV/s.

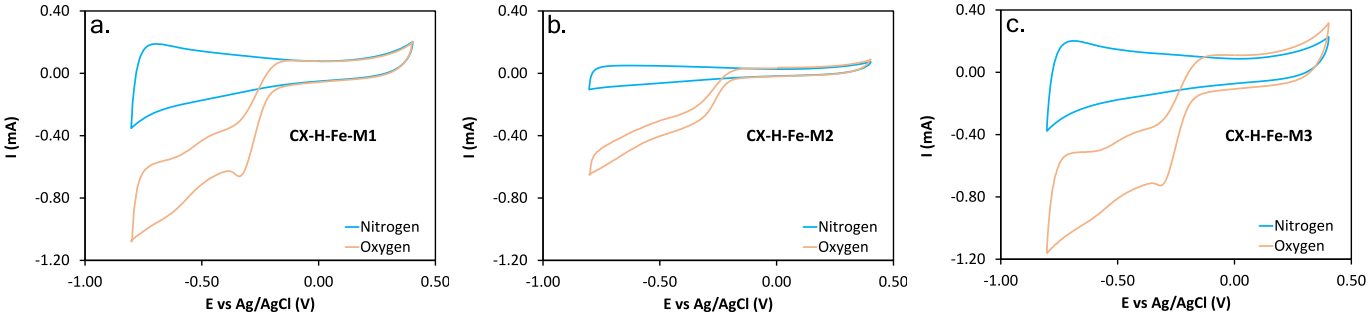

Fig. 10. Cyclic voltammograms at 1000 rpm and 50 mV/s of a) CX-H-Fe-M1, b) CX-H-Fe-M2, c) CX-H-Fe-M3 in N_2 bubbling (orange line) and O_2 bubbling (blue line) 0.1 M KOH solution.

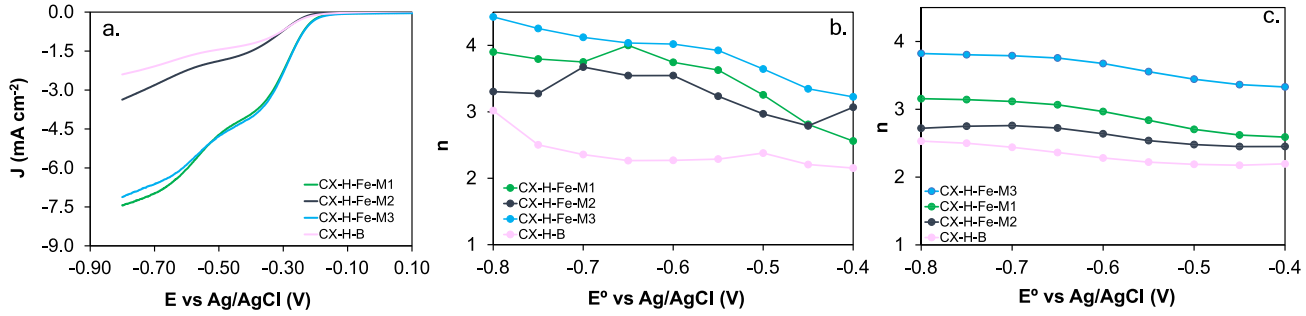

Fig. 11. a) LSV curves for CX-H-Fe-X samples at 3500 rpm b) number of electrons transferred at each potential for all samples. Data obtained from the disc electrode c) number of electrons transferred at each potential. Data obtained from the ring electrode.

Table 1
Electrochemical parameters obtained from the analysis of LSV curves.

Sample	$E_{(onset)}$ V vs Ag/AgCl	−0.45 V			−0.80 V		
		% H_2O_2	J_K (mA/cm^2)	n	% H_2O_2	J_K (mA/cm^2)	n
CX-H-B	−0.23	48.71	1.93	2.01	34.54	4.38	2.03
CX-H-Fe-M1	−0.21	81.51	11.56	3.18	54.70	32.66	4.41
CX-H-Fe-M2	−0.23	77.50	2.43	2.79	53.89	5.87	3.30
CX-H-Fe-M3	−0.21	56.83	11.19	3.35	33.86	28.90	4.43

results obtained in CV and impedance spectroscopy.

A remarkable aspect is that the Jk of the CX-H-Fe-M1 and CX-H-Fe-M3 samples are significantly high, compared to other values reported in the literature under similar conditions. The ORR assay was performed in an electrolyte composed of 0.1 M KOH. (Table 2), which shows that the materials synthesized in this study present enhanced activity for ORR, even at low potentials such as −0.45 V vs Ag/AgCl (Table 1). This could represent a great advantage in terms of energy efficiency, since the use of these materials would allow carrying out the transformation of oxygen into the desired products with lower energy consumption.

To assess the operational stability of the material with the highest Jk (CX-H-Fe-M1), two consecutive chronoamperometry (Fig. 2S) tests were conducted using the same electrode and under the operating conditions intended for the Electro-Fenton system (see Experimental section). The results demonstrate that the recorded current density remains virtually constant and does not vary significantly between the two tests, indicating that the ORR proceeds for at least 16 h of continuous operation without signs of passivation or clogging on the active surface. This suggests that the catalyst maintains its electrocatalytic activity and exhibits no evidence of deactivation over this period, an advantageous property for its application in long-term electrochemical processes.

Once the activity of the materials has been evaluated, the selectivity of each of the samples is analyzed by analyzing the number of electrons involved in the ORR (Fig. 11b). The control sample CX-H-B clearly frames a pathway around two electrons, which remains constant in a potential window of −0.4 to −0.75 V vs Ag/AgCl; due to the spherical morphology of this sample many of the intrinsic defects of the material are more exposed, which can function as active sites facilitating rapid O_2 adsorption [64], allowing protonation of the molecule to become the reaction intermediate $OOH^{\bullet}$ [65], which rapidly transforms to H_2O_2 via 1-electrons (Fig. 12a). It has been found that the selectivity of materials in ORR may be determined by the adsorption energy of the $OOH^{\bullet}$ intermediate, whereby a strong binding strength of the active sites to $OOH^{\bullet}$ enables the reduction of O_2 to H_2O [66–68]. A less strong binding force allows less reduced products to be obtained as is the case for sample CX-H-B.

Regarding the selectivity of the iron-doped samples, CX-H-Fe-M1, CX-H-Fe-M2 and CX-H-Fe-M3, the number of transferred electrons increases around 3 to 4 electrons, depending on the applied potential. The increase in n for these samples may be due to the Fe_3C majority crystalline phases identified in the XRD, which have been characterized as highly active sites for ORR. Fe_3C nanoparticles in addition to increasing O_2 adsorption form a strong interaction with $OOH^{\bullet}$ reaction intermediates, allowing the transfer of more electrons [73–76]. It is interesting to note that in general for Electro-Fenton processes, the desired product of O_2 electro-reduction is H_2O_2 which is obtained by the transfer of two electrons, since, using bifunctional catalysts, or an additional Fenton-type catalyst, H_2O_2 is reduced to $OH^{\bullet}$ responsible for the degradation of contaminants. However, the Fe-doped samples in this study at low potentials such as −0.45 V follow a 3-electron pathway (Table 1). It has been found that three-electron transfer can lead to the direct transformation of intermediates to $OH^{\bullet}$; first the surface adsorbed oxygen is reduced via 1 electron to the intermediate $OOH^{\bullet}$, which via 2 electrons can be reduced to $OH^{\bullet}$. Therefore, the overall reaction from O_2 reduction to $OH^{\bullet}$ is considered a 3-electron pathway as observed in Fig. 12b [69,70,77]. In this case, it is observed that the metallic phase of the iron-doped materials allows a stronger interaction with the adsorbed oxygen, allowing to form at low potentials a binding force with the

Table 2
Comparison of synthesis methodologies and electrochemical performances of carbon-based materials reported in the literature.

Catalyst	Type of metal	Type of material	Preparation method	E_{onset} (V) vs Ag/AgCl	J_k (mAcm^{-2})[d]	Ref
Ni-PANI	Ni (0.70%)[a]	Polymer conducting (Polyaniline)	Copolymerization of melamine and aniline	0.89[c]	5.93	[57]
Pt/C	Pt (20%)	Commercial catalyst	N·I	0.85[c]	5.3	[58]
CK2-Mn-2-10	Mn (7.6%)[b]	Active carbon derived from olive mill	Chemical activation with KOH, post-doping active phase (Manganese Acetate)	N·I	11.37	[15]
PE-Fe	Fe (3.03%)[b]	Carbon derived from Polyethylene (LPDE)	Pyrolysis of low-density polyethylene catalyzed by iron, cobalt or nickel.	−0.2	5.64	[59]
PE-Co	Co (6.65%)[b]			−0.18	10.37	
PE-Ni	Ni (7.84%)[b]			−0.18	4.04	
CoFe/NC	Co, Fe	MOF derives N-hollow carbon	Three steps strategy (corrosion, pyrolysis and replacement reaction)	−0.15[c]	2.00	[60]
Co-NCX	Co (0.07%)[a]	Carbon xerogels	Polymerization and pyrolysis of resorcinol and formaldehyde, curation in vacuum oven for 7 days	−0.21[c]	0.33	[61]
Fe-NCX	Fe (0.11%)[a]			−0.16[c]	0.97	
N-CNT-c	Fe (0.72%)[a]	N-doped carbon nanotubes	Chemical vapor deposition CVD setup	N·I	5.37	[62]
VA-NCNT	metal-free	vertically aligned N-doped carbon nanotubes	Thermal chemical vapor deposition (CVD)	N·I	4.24	[63]
FeCX-0.8	Fe (0.8%)[b]	Carbon xerogel	Polymerization and pyrolysis of resorcinol and formaldehyde, curation 4 days	−0.2	11.11	[37]
CX-H-Fe-M1	Fe (8.40%)[b]	Carbon xerogel	Hydrothermal method, doping with Fe in-situ	−0.21	32.66	This work
CX-H-Fe-M3	Fe (8.83%)[b]	Carbon xerogel		−0.21	28.9	This work

N.I: No information
[a] Metal content obtained by XPS
[b] Metal content obtained by TGA in air
[c] E onset potential vs RHE
[d] Similar conditions: 0.1 M KOH, reporting the Jk at the highest evaluated potential.

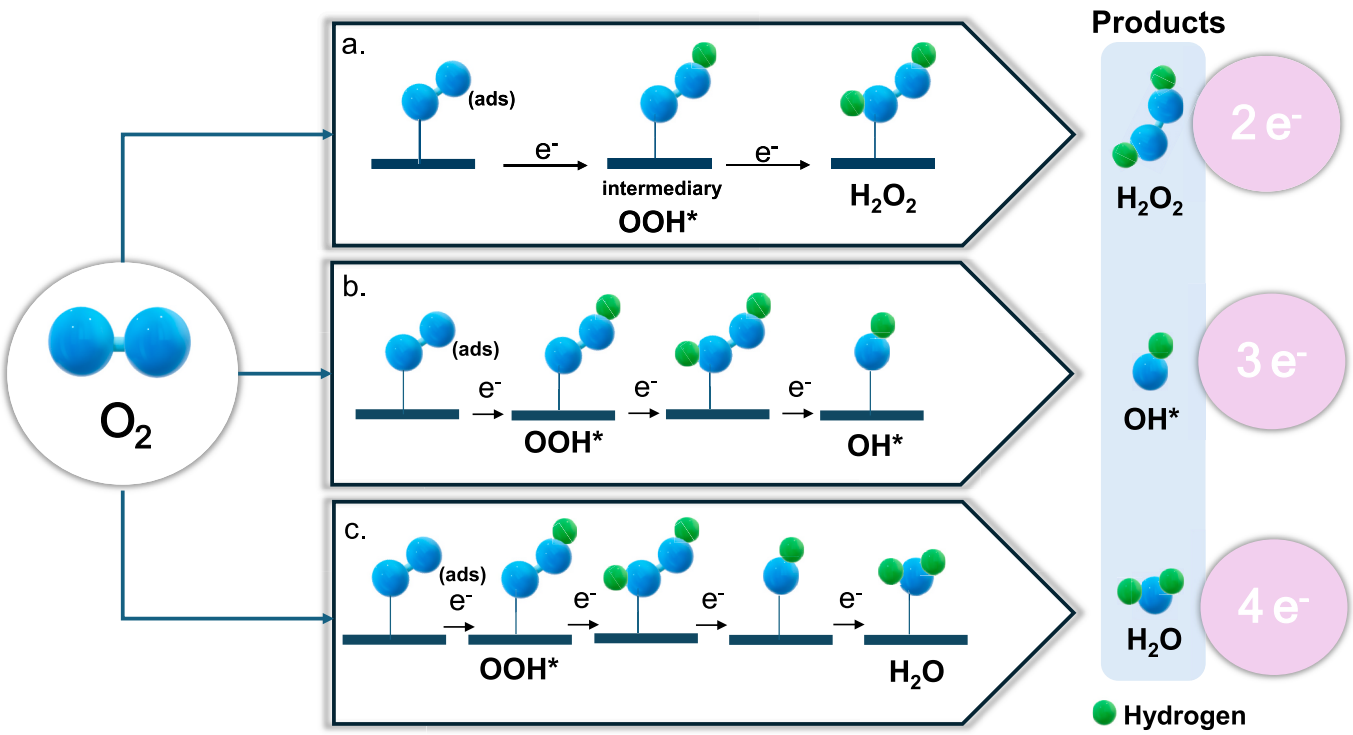

Fig. 12. Proposed reaction mechanism in ORR a) 2-electron pathway, b) 3-electron pathway, c) 4-electron pathway based in [69–72].

OOH● intermediate strong enough to directly obtain OH● radicals. This selectivity towards three-electron transfer may also be in competition with the two- and four-electron selective reactions that give rise to water and peroxide. On the contrary, as the working potential increases, the samples tend to carry the ORR via 4-electrons (Fig. 12c), so that the adsorption energy of the OOH● intermediate becomes much stronger, allowing H_2O to be obtained as the final product. Note that by calculating the number of electrons transferred using the ring electrode data (Fig. 11c), the same behavior is observed for the number of electrons transferred in all samples.

To continue the selectivity study, the H_2O_2 production was analyzed using the data obtained with the ring electrode (Fig. 13a). First, it is observed that in the iron doped samples, in addition to the selectivity towards a 3-electron or 4-electron pathway as discussed above, there is a production of H_2O_2 to a greater or lesser extent depending on the applied potential. This suggests that the materials also follow a 2-electron pathway. This 2-electron pathway could take place at other active sites, such as intrinsic defects in the carbon xerogel materials, as in the case of sample CX-H-B, which allow H_2O_2 generation. In addition, it is observed that the selectivity of sample CX-H-Fe-M3 towards H_2O_2 is much lower, even compared to the control sample, indicating that it is much more selective towards a 3- or even a 4-electron pathway compared to the other samples. Finally, the reaction mechanism was investigated by Tafel analysis (Fig. 13b), which examines the rate-determining steps in electrocatalytic processes, represented by the Tafel slope. The samples CX-H-Fe-M1 and CX-H-Fe-M3 show a slope of 97.6 mV dec^{-1} and 96.1 mV dec^{-1}, respectively, indicating that these materials can easily adsorb the O_2 molecule on the surface and activate it, allowing the reduction of the overpotential [78]; in addition, the above slopes approach the slope of 120 mV dec^{-1}, indicating that the rate-determining step may be the first electron transfer [36,79]. In contrast, the CX-H-Fe-M2 and CX-H-B samples have a very large Tafel slope, indicating lower electrochemical performance and higher overpotential.

So far, the evaluation of the electrochemical performance of the materials in the ORR, gives promising results, especially for the samples

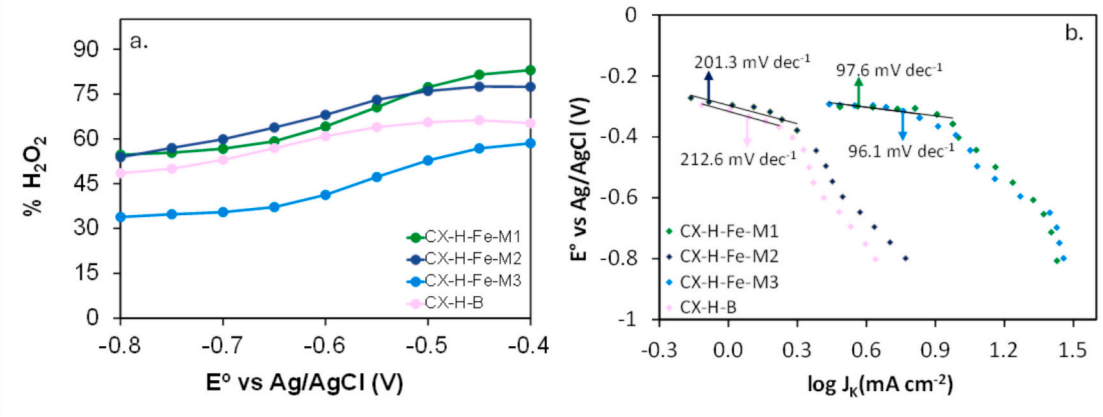

Fig. 13. a) % H_2O_2 produced, b) Tafel plot of specific kinetic current density for CX-H-Fe-X samples.

CX-H-Fe-M1 and CX-H-Fe-M3, which showed superior electrochemical performance, combining high activity, lower overpotential and high selectivity towards the direct production of $OH^{\bullet}$ radicals and/or H_2O_2 production; characteristics that are necessary to be able to apply the materials to the decontamination of water by Electro-Fenton. As for the sample CX-H-F-Fe-M2, although it presented a lower activity and a higher overpotential, it also showed a high selectivity towards a 3-electron and a 2-electron pathway. Therefore, the metal-doped materials will be tested as bifunctional catalysts in Electro-Fenton.

3.3. ORR applied to the Electro-Fenton process

For the Electro-Fenton tests, tetracycline (TTC) was selected as the target antibiotic. -0.45 V vs Ag/AgCl was the working potential selected to carry out the test since, according to the ORR results, at this potential all samples obtain the highest selectivity for a 3-electron pathway and a higher H_2O_2 production combined with a high activity. To accurately attribute the degradation results to the Electro-Fenton process, the adsorption effect was first removed. To do this, the working electrode was saturated in an electrolyte solution containing the pollutant (TTC) at room temperature and in the absence of light, setting after adsorption an initial concentration of 14 mg/L. Once this condition was reached, the reaction was started by applying the selected potential and maintaining a constant bubbling of O_2. The degradation of TTC was observed throughout the reaction time, whose data are presented in Fig. 14.

All samples are capable of degrading TTC; however, the percentage of degradation obtained for each one depends on several factors related to their physicochemical and electrochemical properties. CX-H-Fe-M1 Sample, which obtained the highest percentage of TTC degradation, stands out for combining a high percentage of doped iron and high degree of graphitization, in addition to a micro-mesoporous structure that facilitates the effective transport of reagents and products, allowing high catalytic activity. On the other hand, although sample CX-H-Fe-M3 possesses similar physicochemical properties to sample CX-H-Fe-M1, it obtained a lower percentage of degradation, even lower than that of sample CX-H-Fe-M2 (which showed the worst electrochemical performance). This is because the selectivity towards a 4-electron pathway is higher. Therefore, although it presents excellent electrochemical activity, its selectivity reduces its performance in the Electro-Fenton test. As for sample CX-H-Fe-M2, it obtained a degradation of 74%, an expected result when comparing its properties with sample CX-H-Fe-M1.

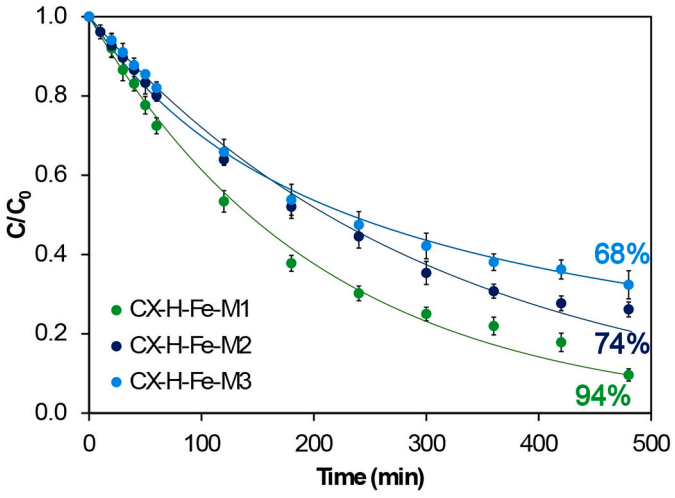

Fig. 14. Normalized TTC concentration vs. time at potential of −0.45 V for CX-H-Fe-X samples, the error bars represent the standard deviation (SD) of the measurements from these replicates and fitting kinetic data: – CX-H-Fe-M1 ($K_1 = 4.88 \times 10^{-3}$ min^{-1}), – CX-H-Fe-M2 ($K_1 = 3.28 \times 10^{-3}$ min^{-1}, – CX-H-Fe-M3 ($K_2 = 2.93 \times 10^{-4}$ L mg^{-1} min^{-1}).

According to the results, the synthesis methods employed allow the formation of Fe_3C particles, which turned out to be excellent active sites for the direct conversion of O_2 to $OH^{\bullet}$. Importantly, these Fe_3C particles are embedded in the matrix of the carbon xerogel, as demonstrated by XPS, which may help to modulate to some extent the selectivity of the samples towards a three-electron pathway.

However, morphology also plays a crucial role. A compact structure without mesoporosity, as seen in CX-H-Fe-M2, can make it difficult for the reactants to reach the active sites. On the contrary, in sample CX-H-Fe-M1, which presented a structure of fused semi-spheres, a greater interaction of the reagents with the embedded Fe_3C nanoparticles was allowed. In this sense, the sample CX-H-Fe-M3, which obtained the most open structure and with a higher mesoporosity, facilitated the access of the reagents to the active sites, allowing a greater interaction of the Fe_3C active phases with oxygen and thus obtaining a higher selectivity towards a four-electron pathway, as demonstrated in the Electron-Fenton tests.

Therefore, two approaches can be explored for future work: first, to deepen synthesis methodology one by studying other types of Fenton-type metals and different percentages of doped metal to improve ORR via three electrons; and second, to consider methodology three to obtain highly active and selective materials for ORR via four electrons, which is highly desirable for application in fuel cells.

On the other hand, to rule out a possible homogeneous contribution in the Electro-Fenton process due to iron leaching, the electrolyte solutions corresponding to the three samples were analyzed at the end of the reaction using ICP-OES. The results showed that the concentration of dissolved iron in all solutions was below the detection limit of the equipment (<0.1 mg/L), suggesting negligible leaching during the process. This finding not only reinforces the hypothesis of a predominantly heterogeneous contribution in the Electro-Fenton process for all samples but also indicates that the coating of the iron nanoparticles with different carbon layers observed by TEM acted as an effective barrier, preventing the release of the metal to the medium.

Additionally, for the best sample (CX-H-Fe-M1), the degree of toxicity of the electrolyte solution was evaluated both before starting and after finishing the Electro-Fenton process. The determination of the toxicity level is a key parameter to assess the possible adverse impacts that the organic compounds present, such as antibiotics, can generate on aquatic organisms and ecosystems. For this purpose, the bacterium *Vibrio fischeri* was used as a bioindicator, whose bioluminescence decreases upon contact with toxic contaminants. This reduction of emitted light is quantified by the percentage of light inhibition (Fig. 4S). In the initial electrolyte solution, 27% inhibition of bioluminescence was observed after 30 min of exposure. However, after treatment by the Electro-Fenton process, this value was significantly reduced to 9.5%, evidenced by a substantial decrease in toxicity. These results confirm that the applied treatment is effective not only in eliminating the TTC antibiotic, but also in mitigating its toxic effects on sensitive aquatic organisms.

Finally, the UV–Vis spectra were analyzed (Fig. 5S), in which two main peaks characteristic of the molecular structure of tetracycline (TTC) were identified, located at approximately 375 nm and 245 nm. These peaks correspond to the presence of aromatic structures, specifically the benzene ring and the fused naphthalene-type rings, respectively [80]. As the reaction Electro-Fenton progresses, a progressive decrease in the intensity of both peaks is observed, suggesting the breakdown of the initial aromatic structures and a possible complete mineralization of the compound, or its transformation into aliphatic intermediates of lower molecular weight. It is important to note that, in the latter case, the residual products do not show toxicity, as evidenced in the toxicity tests performed.

4. Conclusions

Bifunctional electrocatalysts were synthesized by a hydrothermal

synthesis process, which not only allowed a facile fabrication method, but also facilitated the formation of the Fe_3C-type crystalline phase and its subsequent encapsulation in a carbon matrix. These encapsulated phases proved to be highly active for the direct conversion of O_2 into $OH^{\bullet}$ radicals via a 3-electrons. To optimize the process, three synthesis routes were evaluated, of which method 1 proved to be the most efficient. The obtained material, named CX-H-Fe-M1, showed an adequate balance between the degree of graphitization and the presence of micro- and mesopores, which favored a high activity towards the ORR, reaching kinetic current densities of $Jk = 11.56\ mA/cm^2$ at -0.45 V and $Jk = 32.66\ mA/cm^2$ at -0.80 V. The morphology of the material, together with the homogeneous distribution of the encapsulated Fe_3C active phases, allowed an effective modulation of the selectivity towards $OH^{\bullet}$, which resulted in an outstanding performance in the Electro-Fenton process at low potentials such as -0.45 V. In this sense, the catalyst achieved 94% degradation efficiency of the model pollutant TTC, evidencing its potential as a highly efficient bifunctional catalyst. Furthermore, it should be noted that the hydrothermal synthesis employed represents a more sustainable, economical and less complex route for metal encapsulation, which not only reduces the environmental impact, but also opens new perspectives for the rational and scalable design of bifunctional catalysts applicable in advanced oxidation processes such as Electro-Fenton.

CRediT authorship contribution statement

Lilian D. Ramírez-Valencia: Writing – original draft, Methodology, Investigation, Formal analysis, Data curation. **Esther Bailón-García:** Writing – review & editing, Validation, Supervision, Resources, Project administration, Funding acquisition. **Francisco Carrasco-Marín:** Visualization, Methodology, Funding acquisition, Conceptualization. **Miguel A. Álvarez-Merino:** Visualization, Validation, Conceptualization. **Agustín F. Pérez-Cadenas:** Validation, Project administration, Funding acquisition, Data curation, Supervision.

Declaration of competing interest

The authors declare that they have no known competing financial interests or personal relationships that could have appeared to influence the work reported in this paper.

Acknowledgments

The authors acknowledge the support by Grants PID2021-127803OB-I00 and CNS2023-144680 funded by MICIU/AEI/https://doi.org/10.13039/501100011033 and by "ERDF A way of making Europe" and "European Union NextGenerationEU/PRTR", respectively. This article is part of the reference aid DGF_PLSQ_2023_00183 granted by Consejería de Universidad, Investigación e Innovación of the Regional Government of Andalusia, funded by the Andalusia 2021-2027 FEDER Operational Programme. Esther Bailón-García is grateful for her grant RYC2020-029301-I funded by MCIN/AEI/https://doi.org/10.13039/501100011033 and, by "ESF Investing in your future". Lilian D Ramírez-Valencia acknowledge "MINCIENCIAS" for supporting their PhD studies. Funding for open access charge: Universidad de Granada / CBUA.

Appendix A. Supplementary data

Supplementary data to this article can be found online at https://doi.org/10.1016/j.cej.2025.165565.

Data availability

Data will be made available on request.

References

[1] Z. Wang, M. Liu, F. Xiao, G. Postole, H. Zhao, G. Zhao, Recent advances and trends of heterogeneous electro-Fenton process for wastewater treatment-review, Chin. Chem. Lett. 33 (2) (2022) 653–662, https://doi.org/10.1016/j.cclet.2021.07.044.
[2] R.F. Waris, I.H. Farooqi, Different advanced oxidation processes for the abatement of pharmaceutical compounds, Int. J. Environ. Sci. Technol. 21 (2) (2024) 2325–2338, https://doi.org/10.1007/s13762-023-05127-w.
[3] V.M. Almeida, C.A. Orge, M.F.R. Pereira, O.S.G.P. Soares, O3 based advanced oxidation for ibuprofen degradation, Chin. J. Chem. Eng. 42 (2022) 277–284, https://doi.org/10.1016/j.cjche.2021.04.032.
[4] H. Olvera-Vargas, V.Y.H. Wee, O. Garcia-Rodriguez, O. Lefebvre, Near-neutral electro-Fenton treatment of pharmaceutical pollutants: effect of using a triphosphate ligand and BDD electrode, ChemElectroChem 6 (3) (2019) 937–946, https://doi.org/10.1002/celc.201801732.
[5] X.Z. Li, H.S. Liu, Development of an E-H2O2/TiO2 Photoelectrocatalytic oxidation system for water and wastewater treatment, Environ. Sci. Technol. 39 (12) (2005) 4614–4620, https://doi.org/10.1021/es048276k.
[6] Z. Ai, et al., Fe@Fe2O3 Core−Shell nanowires as an Iron reagent. 3. Their combination with CNTs as an effective oxygen-fed gas diffusion electrode in a neutral electro-Fenton system, J. Phys. Chem. C 111 (40) (2007) 14799–14803, https://doi.org/10.1021/jp073617c.
[7] G. Matyszczak, K. Krzyczkowska, A. Fidler, A novel, two-electron catalysts for the electro-Fenton process, Journal of Water Process Engineering 36 (2020) 101242, https://doi.org/10.1016/j.jwpe.2020.101242.
[8] N. Daneshvar, S. Aber, V. Vatanpour, M.H. Rasoulifard, Electro-Fenton treatment of dye solution containing Orange II: influence of operational parameters, J. Electroanal. Chem. 615 (2) (2008) 165–174, https://doi.org/10.1016/j.jelechem.2007.12.005.
[9] L. Labiadh, M.A. Oturan, M. Panizza, N. Ben Hamadi, S. Ammar, Complete removal of AHPS synthetic dye from water using new electro-Fenton oxidation catalyzed by natural pyrite as heterogeneous catalyst, J. Hazard. Mater. 297 (2015) 34–41, https://doi.org/10.1016/j.jhazmat.2015.04.062.
[10] C.-Y. Chen, et al., Oxygen reduction reaction on graphene in an electro-fenton system: in situ generation of H2O2 for the oxidation of organic compounds, ChemSusChem 9 (10) (2016) 1194–1199, https://doi.org/10.1002/cssc.201600030.
[11] J. Zhao, X. Quan, S. Chen, H. Yu, N-doped three-dimensional carbon foam as binder-free electrode for organic pollutants removal by electro-Fenton in neutral medium, Blue-Green Systems 1 (1) (2019) 86–101, https://doi.org/10.2166/bgs.2019.911.
[12] S. Jiang, Y. Han, B. Sun, L. Zeng, J. Gong, Reduced sulfur accelerates Fe(III)/Fe(II) recycling in FeS2 surface for enhanced electro-Fenton reaction, Chemosphere 353 (2024) 141588, https://doi.org/10.1016/j.chemosphere.2024.141588.
[13] E. Fajardo-Puerto, et al., Bifunctional catalysts based on carbon-coated manganese microspheres applied in the heterogeneous electro-Fenton process for tetracycline degradation, J. Environ. Chem. Eng. 13 (2) (2025) 115725, https://doi.org/10.1016/j.jece.2025.115725.
[14] L.D. Ramírez-Valencia, E. Bailón-García, A.I. Moral-Rodríguez, F. Carrasco-Marín, A.F. Pérez-Cadenas, Carbon gels–green graphene composites as metal-free bifunctional electro-fenton catalysts, Gels 9 (8) (2023), https://doi.org/10.3390/gels9080665.
[15] E. Fajardo-Puerto, A. Elmouwahidi, E. Bailón-García, M. Pérez-Cadenas, A.F. Pérez-Cadenas, F. Carrasco-Marín, Antibiotic degradation via Fenton process assisted by a 3-Electron oxygen reduction reaction pathway catalyzed by bio-carbon–manganese composites, Nanomaterials 14 (13) (2024), https://doi.org/10.3390/nano14131112.
[16] E. Fajardo-Puerto, et al., Size control of carbon Xerogel spheres as key factor governing the H2O2 selectivity in metal-free bifunctional electro-Fenton catalysts for tetracycline degradation, Gels 10 (5) (2024), https://doi.org/10.3390/gels10050306.
[17] Y. Ding, et al., Pulsed electrocatalysis enables the stabilization and activation of carbon-based catalysts towards H2O2 production, Appl Catal B 316 (2022) 121688, https://doi.org/10.1016/j.apcatb.2022.121688.
[18] Q. Zhai, et al., Recent advances on carbon-based metal-free Electrocatalysts for energy and chemical conversions, Adv. Mater. 36 (42) (2024) 2405664, https://doi.org/10.1002/adma.202405664.
[19] S. Li, Z. Zhu, Y. Zhang, Y. Liu, X. Zhang, K.N. Hui, Innovative engineering strategies and mechanistic insights for enhanced carbon-based electrocatalysts in sustainable H2O2 production, Mater. Horiz. (2025), https://doi.org/10.1039/D5MH00221D.
[20] Q. Ye, T.N. Hunter, H. Xu, D. Harbottle, G.M. Kale, M.R. Tillotson, CuCo carbon aerogel as a bifunctional cathode for electro-Fenton processes: unveiling synergistic effects and catalytic mechanisms, Sep. Purif. Technol. 361 (2025) 131597, https://doi.org/10.1016/j.seppur.2025.131597.
[21] Y. Liu, Z. Yang, J. Wang, Fenton-like degradation of sulfamethoxazole in Cu0/Zn0-air system over a broad pH range: performance, kinetics and mechanism, Chem. Eng. J. 403 (2021) 126320, https://doi.org/10.1016/j.cej.2020.126320.
[22] S. Cheng, et al., FeCo-ZIF derived carbon-encapsulated metal alloy as efficient cathode material for heterogeneous electro-Fenton reaction in 3-electron ORR pathway: enhanced performance in alkaline condition, Sep. Purif. Technol. 325 (2023) 124545, https://doi.org/10.1016/j.seppur.2023.124545.
[23] Y. Yao, et al., Bifunctional catalysts for heterogeneous electro-Fenton processes: a review, Environ. Chem. Lett. 20 (6) (2022) 3837–3859, https://doi.org/10.1007/s10311-022-01453-6.
[24] C. Wang, P. Shi, C. Guo, R. Guo, J. Qiu, CuCo2O4/CF cathode with bifunctional and dual reaction centers exhibits high RhB degradation in electro-Fenton systems,

J. Electroanal. Chem. 956 (2024) 118072, https://doi.org/10.1016/j.jelechem.2024.118072.
[25] S. Cheng, H. Zheng, C. Shen, B. Jiang, F. Liu, A. Li, Hierarchical Iron phosphides composite confined in ultrathin carbon layer as effective heterogeneous electro-Fenton catalyst with prominent stability and catalytic activity, Adv. Funct. Mater. 31 (48) (2021) 2106311, https://doi.org/10.1002/adfm.202106311.
[26] X. Huang, Y. Niu, W. Hu, Fe/Fe3C nanoparticles loaded on Fe/N-doped graphene as an efficient heterogeneous Fenton catalyst for degradation of organic pollutants, Colloids Surf. A Physicochem. Eng. Asp. 518 (2017) 145–150, https://doi.org/10.1016/j.colsurfa.2017.01.039.
[27] Y. Wang, Y. Xue, C. Zhang, Copper embedded in nitrogen-doped carbon matrix derived from metal-organic frameworks for boosting peroxide production and electro-Fenton catalysis, Electrochim. Acta 368 (2021) 137643, https://doi.org/10.1016/j.electacta.2020.137643.
[28] Y. Yang, L. Xu, W. Li, W. Fan, S. Song, J. Yang, Adsorption and degradation of sulfadiazine over nanoscale zero-valent iron encapsulated in three-dimensional graphene network through oxygen-driven heterogeneous Fenton-like reactions, Appl Catal B 259 (2019) 118057, https://doi.org/10.1016/j.apcatb.2019.118057.
[29] P. Su, W. Fu, Z. Hu, J. Jing, M. Zhou, Insights into transition metal encapsulated N-doped CNTs cathode for self-sufficient electrocatalytic degradation, Appl Catal B 313 (2022) 121457, https://doi.org/10.1016/j.apcatb.2022.121457.
[30] Z. Han, et al., Enhanced electron transfer and hydrogen peroxide activation capacity with N, P-codoped carbon encapsulated CeO2 in heterogeneous electro-Fenton process, Chemosphere 287 (2022) 132154, https://doi.org/10.1016/j.chemosphere.2021.132154.
[31] Y. Amangelsin, Y. Semenova, M. Dadar, M. Aljofan, G. Bjørklund, The impact of tetracycline pollution on the aquatic environment and removal strategies, Antibiotics 12 (3) (2023), https://doi.org/10.3390/antibiotics12030440.
[32] O. Hosu, G. Melinte, G. Ştefan, M. Casian, C. Cristea, Towards selective tetracycline recognition in wastewater based on gold nanovoids@aptamer sensing, Electrochim. Acta 460 (2023) 142556, https://doi.org/10.1016/j.electacta.2023.142556.
[33] J. Boisseau, Basis for the evaluation of the microbiological risks due to veterinary drug residues in food, Vet. Microbiol. 35 (3) (1993) 187–192, https://doi.org/10.1016/0378-1135(93)90143-U.
[34] F. Wang, Z. Wang, Y. Zhao, J. Zhang, Performance of traditional and emerging water-treatment Technologies in the Removal of tetracycline antibiotics, Catalysts 14 (4) (2024), https://doi.org/10.3390/catal14040269.
[35] G. Yan, et al., N-carbon coated P-W2C composite as efficient electrocatalyst for hydrogen evolution reactions over the whole pH range, J. Mater. Chem. A 5 (2) (2017) 765–772, https://doi.org/10.1039/C6TA09052D.
[36] A. Elmouwahidi, E. Bailón-García, A.F. Pérez-Cadenas, J. Castelo-Quibén, F. Carrasco-Marín, Carbon-vanadium composites as non-precious catalysts for electro-reduction of oxygen, Carbon N Y 144 (2019) 289–300, https://doi.org/10.1016/j.carbon.2018.12.038.
[37] A. Barranco-López, A.I. Moral-Rodríguez, E. Fajardo-Puerto, A. Elmouwahidi, E. Bailón-García, Highly graphitic Fe-doped carbon xerogels as dual-functional electro-Fenton catalysts for the degradation of tetracycline in wastewater, Environ. Res. 228 (2023) 115757, https://doi.org/10.1016/j.envres.2023.115757.
[38] X. Zhao, M. Zhang, X. Sun, X. Li, J. Li, Comprehensive understanding of the formation process on monodisperse resorcinol-formaldehyde polymer and carbon spheres and their use as substrates for surface-enhanced Raman spectroscopy, Appl. Surf. Sci. 506 (2020) 144591, https://doi.org/10.1016/j.apsusc.2019.144591.
[39] X.-L. Dong, et al., Synthetic porous carbons for clean energy storage and conversion, EnergyChem 5 (4) (2023) 100099, https://doi.org/10.1016/j.enchem.2023.100099.
[40] T. Hosseinzadeh Sanatkar, A. Khorshidi, R. Yaghoubi, E. Sohouli, J. Shakeri, Stöber synthesis of salen-formaldehyde resin polymer- and carbon spheres with high nitrogen content and application of the corresponding Mn-containing carbon spheres as efficient electrocatalysts for the oxygen reduction reaction, RSC Adv. 10 (46) (2020) 27575–27584, https://doi.org/10.1039/D0RA03815F.
[41] P. Zhang, Z.-A. Qiao, S. Dai, Recent advances in carbon nanospheres: synthetic routes and applications, Chem. Commun. 51 (45) (2015) 9246–9256, https://doi.org/10.1039/C5CC01759A.
[42] C. Moreno-Castilla, H. García-Rosero, F. Carrasco-Marín, Synthesis and characterization of solid polymer and carbon spheres derived from an emulsion polymerization reaction of different phenolic compounds with formaldehyde, Colloids Surf. A Physicochem. Eng. Asp. 520 (2017) 488–496, https://doi.org/10.1016/j.colsurfa.2017.02.021.
[43] J. Liu, et al., Extension of the stöber method to the preparation of monodisperse resorcinol–formaldehyde resin polymer and carbon spheres, Angew. Chem. Int. Ed. 50 (26) (2011) 5947–5951, https://doi.org/10.1002/anie.201102011.
[44] J. Castelo-Quibén, et al., Carbon - iron electro-catalysts for CO2 reduction. The role of the iron particle size, Journal of CO2 Utilization 24 (2018) 240–249, https://doi.org/10.1016/j.jcou.2018.01.007.
[45] E.P. Sajitha, V. Prasad, S.V. Subramanyam, A.K. Mishra, S. Sarkar, C. Bansal, Size-dependent magnetic properties of iron carbide nanoparticles embedded in a carbon matrix, J. Phys. Condens. Matter 19 (4) (2007) 46214, https://doi.org/10.1088/0953-8984/19/4/046214.
[46] Q.-D. Ruan, R. Feng, J.-J. Feng, Y.-J. Gao, L. Zhang, A.-J. Wang, High-activity Fe3C as pH-universal Electrocatalyst for boosting oxygen reduction reaction and zinc-air battery, Small 19 (27) (2023) 2300136, https://doi.org/10.1002/smll.202300136.
[47] Y. Wang, D.C. Alsmeyer, R.L. McCreery, Raman spectroscopy of carbon materials: structural basis of observed spectra, Chem. Mater. 2 (5) (1990) 557–563, https://doi.org/10.1021/cm00011a018.
[48] J.-M. Vallerot, X. Bourrat, A. Mouchon, G. Chollon, Quantitative structural and textural assessment of laminar pyrocarbons through Raman spectroscopy, electron diffraction and few other techniques, Carbon N Y 44 (9) (2006) 1833–1844, https://doi.org/10.1016/j.carbon.2005.12.029.
[49] D.B. Schuepfer, et al., Assessing the structural properties of graphitic and non-graphitic carbons by Raman spectroscopy, Carbon N Y 161 (2020) 359–372, https://doi.org/10.1016/j.carbon.2019.12.094.
[50] Y. Zhu, K. Lv, X. Wang, H. Yang, G. Xiao, Y. Zhu, 1D/2D nitrogen-doped carbon nanorod arrays/ultrathin carbon nanosheets: outstanding catalysts for the highly efficient electroreduction of CO2 to CO, J. Mater. Chem. A 7 (24) (2019) 14895–14903, https://doi.org/10.1039/C9TA02353D.
[51] V. Sunil, B. Pal, I. Izwan Misnon, R. Jose, Characterization of supercapacitive charge storage device using electrochemical impedance spectroscopy, Mater Today Proc 46 (2021) 1588–1594, https://doi.org/10.1016/j.matpr.2020.07.248.
[52] B.-A. Mei, O. Munteshari, J. Lau, B. Dunn, L. Pilon, Physical interpretations of Nyquist plots for EDLC electrodes and devices, J. Phys. Chem. C 122 (1) (2018) 194–206, https://doi.org/10.1021/acs.jpcc.7b10582.
[53] X. Jing, et al., KOH chemical-activated porous carbon sponges for monolithic supercapacitor electrodes, ACS Appl Energy Mater 4 (7) (2021) 6768–6776, https://doi.org/10.1021/acsaem.1c00868.
[54] L.D. Ramírez-Valencia, F.E. López-Suárez, L.R. Conde, Esther Bailón-García, A. Bueno-López, A.F. Perez-Cadenas, Cocoa husk as precursor of carbonaceous materials for supercapacitors electrodes, J. Electroanal. Chem. 963 (2024) 118325, https://doi.org/10.1016/j.jelechem.2024.118325.
[55] M.M. Radhi, E.A. Jaffar Al-Mulla, W.T. Tan, Electrochemical characterization of the redox couple of Fe(III)/Fe(II) mediated by grafted polymer electrode, Res. Chem. Intermed. 40 (1) (2014) 179–192, https://doi.org/10.1007/s11164-012-0954-6.
[56] S.-Y. Lin, L.-X. Xia, L. Zhang, J.-J. Feng, Y. Zhao, A.-J. Wang, Highly active Fe centered FeM-N-doped carbon (M = Co/Ni/Mn): a general strategy for efficient oxygen conversion in Zn–air battery, Chem. Eng. J. 424 (2021) 130559, https://doi.org/10.1016/j.cej.2021.130559.
[57] H. Peng, et al., Effect of transition metals on the structure and performance of the doped carbon catalysts derived from polyaniline and melamine for ORR application, ACS Catal. 4 (10) (2014) 3797–3805, https://doi.org/10.1021/cs500744x.
[58] G. Chen, et al., Zinc-mediated template synthesis of Fe-N-C Electrocatalysts with densely accessible Fe-N active sites for efficient oxygen reduction, Adv. Mater. 32 (8) (2020) 1907399, https://doi.org/10.1002/adma.201907399.
[59] J. Castelo-Quibén, E. Bailón-García, A.I. Moral-Rodríguez, F. Carrasco-Marín, A. F. Pérez-Cadenas, Recycling and valorization of LDPE: direct transformation into highly ordered doped-carbon materials and their application as electro-catalysts for the oxygen reduction reaction, Cat. Sci. Technol. 12 (4) (2022) 1187–1201, https://doi.org/10.1039/D1CY02082J.
[60] Y. Jing, Y. Cheng, L. Wang, Y. Liu, B. Yu, C. Yang, MOF-derived Co, Fe, and Ni co-doped N-enriched hollow carbon as efficient electrocatalyst for oxygen reduction reaction, Chem. Eng. J. 397 (2020) 125539, https://doi.org/10.1016/j.cej.2020.125539.
[61] S. Liu, C. Deng, L. Yao, H. Zhong, H. Zhang, The key role of metal dopants in nitrogen-doped carbon xerogel for oxygen reduction reaction, J. Power Sources 269 (2014) 225–235, https://doi.org/10.1016/j.jpowsour.2014.06.148.
[62] Z. Chen, D. Higgins, Z. Chen, Nitrogen doped carbon nanotubes and their impact on the oxygen reduction reaction in fuel cells, Carbon N Y 48 (11) (2010) 3057–3065, https://doi.org/10.1016/j.carbon.2010.04.038.
[63] S. Wang, E. Iyyamperumal, A. Roy, Y. Xue, D. Yu, L. Dai, Vertically aligned BCN nanotubes as efficient metal-free Electrocatalysts for the oxygen reduction reaction: a synergetic effect by co-doping with boron and nitrogen, Angew. Chem. Int. Ed. 50 (49) (2011) 11756–11760, https://doi.org/10.1002/anie.201105204.
[64] X. Qin, K. Zhao, X. Quan, P. Cao, S. Chen, H. Yu, Highly efficient metal-free electro-Fenton degradation of organic contaminants on a bifunctional catalyst, J. Hazard. Mater. 416 (2021) 125859, https://doi.org/10.1016/j.jhazmat.2021.125859.
[65] K. Jiang, et al., Highly selective oxygen reduction to hydrogen peroxide on transition metal single atom coordination, Nat. Commun. 10 (1) (2019) 3997, https://doi.org/10.1038/s41467-019-11992-2.
[66] Z. Lu, et al., High-efficiency oxygen reduction to hydrogen peroxide catalysed by oxidized carbon materials, Nat. Catal. 1 (2) (2018) 156–162, https://doi.org/10.1038/s41929-017-0017-x.
[67] C. Tang, et al., Coordination Tunes selectivity: two-Electron oxygen reduction on high-loading molybdenum single-atom catalysts, Angew. Chem. Int. Ed. 59 (23) (2020) 9171–9176, https://doi.org/10.1002/anie.202003842.
[68] S. Chen, et al., Defective carbon-based materials for the electrochemical synthesis of hydrogen peroxide, ACS Sustain. Chem. Eng. 6 (1) (2018) 311–317, https://doi.org/10.1021/acssuschemeng.7b02517.
[69] Y. Yao, et al., Bifunctional catalysts for heterogeneous electro-Fenton processes: a review, Environ. Chem. Lett. 20 (6) (2022) 3837–3859, https://doi.org/10.1007/s10311-022-01453-6.
[70] F. Xiao, Z. Wang, J. Fan, T. Majima, H. Zhao, G. Zhao, Selective Electrocatalytic reduction of oxygen to hydroxyl radicals via 3-Electron pathway with FeCo alloy encapsulated carbon aerogel for fast and complete removing pollutants, Angew. Chem. Int. Ed. 60 (18) (2021) 10375–10383, https://doi.org/10.1002/anie.202101804.
[71] J.-M. Noël, A. Latus, C. Lagrost, E. Volanschi, P. Hapiot, Evidence for OH radical production during Electrocatalysis of oxygen reduction on Pt surfaces: consequences and application, J. Am. Chem. Soc. 134 (5) (2012) 2835–2841, https://doi.org/10.1021/ja211663t.

[72] Z. Wang, N. Hu, L. Wang, H. Zhao, G. Zhao, In situ production of hydroxyl radicals via three-Electron oxygen reduction: opportunities for water treatment, Angew. Chem. Int. Ed. 63 (40) (2024) e202407628, https://doi.org/10.1002/anie.202407628.
[73] T.Y. Burshtein, et al., Fe–N–C electrocatalysts in the oxygen and nitrogen cycles in alkaline media: the role of iron carbide, Phys. Chem. Chem. Phys. 23 (47) (2021) 26674–26679, https://doi.org/10.1039/D1CP03650E.
[74] M. Liu, et al., Fe3O4/Fe3C@nitrogen-doped carbon for enhancing oxygen reduction reaction, ChemNanoMat 5 (2) (2019) 187–193, https://doi.org/10.1002/cnma.201800432.
[75] F. Zhou, P. Yu, F. Sun, G. Zhang, X. Liu, L. Wang, The cooperation of Fe3C nanoparticles with isolated single iron atoms to boost the oxygen reduction reaction for Zn–air batteries, J. Mater. Chem. A 9 (11) (2021) 6831–6840, https://doi.org/10.1039/D1TA00039J.
[76] Q.-D. Ruan, R. Feng, J.-J. Feng, Y.-J. Gao, L. Zhang, A.-J. Wang, High-activity Fe3C as pH-universal Electrocatalyst for boosting oxygen reduction reaction and zinc-air battery, Small 19 (27) (2023) 2300136, https://doi.org/10.1002/smll.202300136.
[77] J.-M. Noël, A. Latus, C. Lagrost, E. Volanschi, P. Hapiot, Evidence for OH radical production during electrocatalysis of oxygen reduction on Pt surfaces: consequences and application, J. Am. Chem. Soc. 134 (5) (2012) 2835–2841, https://doi.org/10.1021/ja211663t.
[78] M.P. Araújo, M. Nunes, I.M. Rocha, M.F.R. Pereira, C. Freire, Electrocatalytic activity of new Mn3O4@oxidized graphene flakes nanocomposites toward oxygen reduction reaction, J. Mater. Sci. 54 (12) (2019) 8919–8940, https://doi.org/10.1007/s10853-019-03508-6.
[79] R.L. Doyle, M.E.G. Lyons, The oxygen evolution reaction: mechanistic concepts and catalyst design, in: S. Giménez, J. Bisquert (Eds.), Photoelectrochemical Solar Fuel Production: From Basic Principles to Advanced Devices, Springer International Publishing, Cham, 2016, pp. 41–104, https://doi.org/10.1007/978-3-319-29641-8_2.
[80] S. Chen, et al., Carbon felt cathodes for electro-Fenton process to remove tetracycline via synergistic adsorption and degradation, Sci. Total Environ. 670 (2019) 921–931, https://doi.org/10.1016/j.scitotenv.2019.03.086.